Aeroelastic Wind Tunnel Testing of Yawed Wind Turbine Rotor with Teetering Hub

Tsatsas, I.; Georgopoulos, P.; Sodja, J.; De Breuker, R.

DOI
10.2514/6.2024-1701

Publication date
2024

Document Version
Final published version

Published in
Proceedings of the AIAA SCITECH 2024 Forum

AIAA SciTech Forum
8-12 January 2024, Orlando, FL
AIAA SCITECH 2024 Forum

10.2514/6.2024-1701

Aeroelastic Wind Tunnel Testing of Yawed Wind Turbine Rotor with Teetering Hub

Ilias Tsatsas*, Panagiotis Georgopoulos†, Jurij Sodja‡ and Roeland De Breuker§
Delft University of Technology, Faculty of Aerospace Engineering, Kluyverweg 1, Delft, 2629 HS, The Netherlands

This paper presents an experimental investigation into the aeroelastic behavior of an innovative wind turbine design featuring a downwind two-blade rotor with a teetering hub mounted on a tower with adjustable tilt. The rotor model incorporates two sets of elastic blades—stiff and flexible—for scaling purposes, each instrumented with strain gauges and accelerometers. Ground and wind tunnel tests were conducted to analyze the aeroelastic response. Static tests exhibited discrepancies between measured and numerically predicted displacements, with maximum displacements near the tip exceeding numerical predictions by 14% and 31% for flexible and stiff blades respectively. Frequency differences between measured and numerically simulated elastic modes ranged from 0.5% to 18% for both blade sets, as determined by ground vibration tests. Wind tunnel tests revealed the dominance of rotational speed harmonics, particularly the second harmonic, in the blades' periodic response. A sensitivity analysis was also carried out with respect to tower tilt angle, rotational speed and blade pitch angle, for both blade sets at a range of tip-speed ratio values. The static response of the system, as captured by the generated power and thrust, was primarily sensitive to tower tilt angle variation and to a lesser extent blade pitch angle. Conversely, the tip-speed ratio in conjunction with rotational speed were found to dictate the dynamic response, influencing the azimuthal position and magnitude of the maximum bending moment at the blade root. Finally, no dynamic aeroelastic instability was observed during wind tunnel tests.

I. Nomenclature

a_{zt}	=	blade tip acceleration, m/s^2
C_P	=	power coefficient
C_T	=	thrust coefficient
$\vec{f_A}$	=	aerodynamic force, N
$\vec{f_{A,p}}$	=	periodic component of aerodynamic force, N
$\vec{f_{A,t}}$	=	turbulence component of aerodynamic force, N
$\vec{f_{A,0}}$	=	static component of aerodynamic force, N
f_z	=	applied shear force, N
M_x	=	blade root bending moment, $N{\cdot}m$
$M_{x,ref}$	=	reference blade root bending moment, $N{\cdot}m$
$M_{x,p}$	=	periodic component of blade root bending moment, $N{\cdot}m$
$M_{x,0}$	=	static component of blade root bending moment, $N{\cdot}m$
M_y	=	blade root torsion moment, $N{\cdot}m$
m_y	=	applied torsion moment, $N{\cdot}m$
q	=	modal amplitude, m
t	=	time, s
$\vec{v}$	=	elastic mode shape

*Researcher, Faculty of Aerospace Engineering, Aerospace Structures and Materials, Kluyverweg 1, 2629 HS, Delft, i.tsatsas@tudelft.nl
†PhD candidate, Faculty of Aerospace Engineering, Aerospace Structures and Materials, Kluyverweg 1, 2629 HS, Delft, p.georgopoulos@tudelft.nl, AIAA Student Member
‡Assistant Professor, Faculty of Aerospace Engineering, Aerospace Structures and Materials, Kluyverweg 1, 2629 HS, Delft, j.sodja@tudelft.nl, AIAA Senior Member
§Associate Professor, Faculty of Aerospace Engineering, Aerospace Structures and Materials, Kluyverweg 1, 2629 HS, Delft, r.debreuker@tudelft.nl, AIAA Associate Fellow

$\vec{x}$ = displacement, m
$\vec{x_p}$ = displacement due to periodic excitation, m
$\vec{x_t}$ = displacement due to turbulence excitation, m
$\vec{x_0}$ = displacement due to static excitation, m
β = blade pitch angle, °
γ = rotor yaw angle, °
$\Delta\theta$ = torsional rotation, °
Δz = flapwise displacement, m
Δz_{el} = elastic component of flapwise displacement, m
Δz_{rot} = rotational component of flapwise displacement, m
δ_3 = hinge delta-3 angle , °
λ = tip speed ratio
ξ = tower tilt angle, °
τ = modal phase angle, °
ϕ = rotor azimuthal position, °
Ω = rotational speed, *RPM*

II. Introduction

WIND energy harnessing is one of the most promising options for decarbonizing electrical energy production. There are certain challenges, however, in the shift from fossil-fuels to renewable zero-emission sources. In the context of wind energy, on-shore wind-parks are often facing the challenge of limited land availability, as well as rising concerns from the local communities regarding their environmental impact, including wildlife disruption, visual pollution [1] and noise [2]. Consequently, there is an increasing interest in off-shore wind turbines.

Recent research has focused on the development of floating offshore wind turbine (FOWT) systems, to exploit more extensive off-shore regions, where water is deeper than 60m. Studies have proposed various configurations for their floating supports, such as the Tension Leg Platform, Spar Buoy and Semi-Submersible [3] as well as different rotor designs, including: Darrieus and V-type vertical axis wind turbines (VAWTs) [4].

In response to this demand, TouchWind BV has introduced a novel FOWT concept [5]. Its characteristic features include a two-blade rotor, a teetering hub that passively adjusts blade pitch, a variable tilt angle tower that passively adjusts the rotor's yaw angle and a cylindrical floater support Fig.1. The primary objective is to reduce cost by using a one-piece rotor and a light-weight tower capable of adjusting rotor's yaw angle in high wind conditions, with the goal of keeping the system operational when conventional horizontal axis wind turbines (HAWTs) would halt operation. In addition, tilted rotors are hypothesized to increase wind park efficiency by deflecting the wake downwards and pulling higher velocity air from the upper layers of the atmospheric boundary layer; validating this effect is the focus of the ongoing "POsitive Wake Effects of turbines with tilted Rotors" (POWER) project [6].

According to Civati et al.[2], two-blade rotors, due to their cost-effectiveness, can achieve large dimensions and should operate at high tip speed ratios λ owing to their low solidity. Combining the above with the use of lightweight flexible materials [7] and the potential coupling of rotor and floating support dynamics [8], an aeroelastic study of the TouchWind concept rotor becomes critical. In literature, a small number of experimental studies concerning the aeroelastic behaviour of wind turbines can be found, primarily relying upon measurements from strain gauges placed on the tower [8, 9] or at the blade root [8]. In this study, strain gauges on the blade root are combined with accelerometers in the flapwise and edgewise direction, to further investigate the rotor's dynamic response and stability.

The first step in the aeroelastic analysis of the TouchWind concept was made by its aerodynamic model development. Krishnan et al. [10] coupled a blade element momentum (BEM) approach to a rigid body model of the rotor, with a teetering hub. They found that the delta-3 hinge mechanism balances the aerodynamic loads between the advancing and retreating blade. A parallel study by Georgopoulos et al. [11] proposed a reduced order model (ROM) for the equations of motion (EoM) in order to predict the natural frequencies and flexible modes of the 30m full-scale rotor. In addition, they proposed a scaling strategy for the wind tunnel (WT) model of that rotor. Since a single rotor could not match all the idnetified scaling parameters, the construction of two distinct rotors was recommended; one with stiff blades that match the natural frequencies and another with flexible blades that match the reference displacement [11].

This study presents an aeroelastic WT testing campaign for a scaled model of the TouchWind wind turbine, using the blades designed by [11]. The tests were performed in the Open Jet Facility (OJF) of TU Delft. Section III introduces the rationale behind the blades' detailed design and rig instrumentation. Section IV presents a ground testing campaign

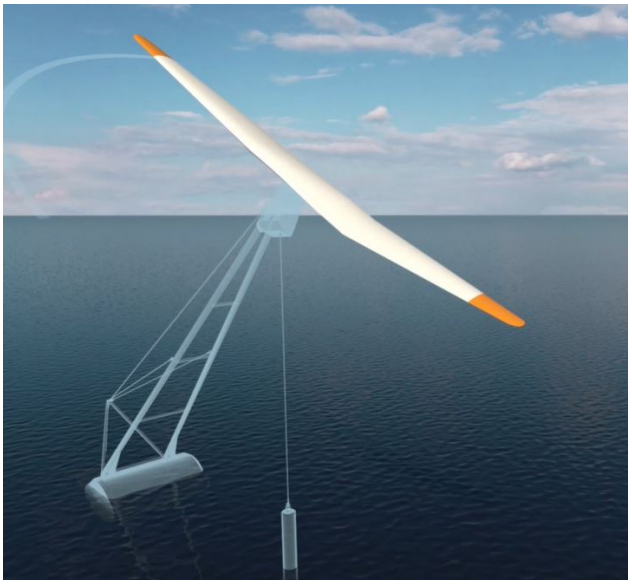

Fig. 1 Touchwind conceptual design[5]

with the purpose of comparing the static and dynamic structural response of the rotor to the numerical model predictions. Section V presents results from the WT tests. Initially, the system's functionality is discussed, comparing the differences between a free and a fixed hinge configuraton. Then, a parametric sensitivity study is presented where the blade pair, tower tilt angle ξ, rotational speed Ω and blade pitch angle β were allowed to vary. The results focus on the power, load and vibration characteristics of the two proposed rotors, for a range of λ values. Section VI summarizes the main conclusions of the study.

III. Experimental Set Up and Instrumentation

Two different pairs of blades were fitted to the metallic hub of the rotor: the stiff and the flexible. The differences in their sections are shown in Fig.2. The need for two separate pairs of blades arose from the inability to match the Lock number of the full-scale rotor used as reference, as that would require an unattainable lightweight blade design, whose features would violate minimum wall thickness requirements[11]. Therefore, the stiff blades were designed to capture vibration behaviour by matching most of the normalised natural frequencies. In contrast, the flexible blades captured blade stiffness by matching the normalised static displacement.

(a) Stiff **(b) Flexible**

Fig. 2 Blade sections (reproduced with permission from [11])

In terms of quantities of interest, the first identified discipline was aerodynamics, the effects of lift being mainly represented by the thrust coefficient C_T, while the combined effects of lift and drag were captured through the resulting torque in the power coefficient C_P. The second discipline was structural mechanics, further split into statics and dynamics. In the case of statics, given space and slip ring channel limitations, it was decided to only monitor the loads at the blade root. The above limitations also prohibited dynamic shape reconstruction, which would require multiple accelerometers. Instead, three accelerometers were used to monitor dynamic stability. The hardware can be allocated in two main categories: the rotor and the rig.

A. Rotor

Two sets of blades were built and instrumented for the WT testing campaign, as shown in Fig.3. The Nylon-12 blade chassis was 3D-printed via selective laser sintering and then wrapped with Oralight foil, imparting the desired aerodynamic shape. Additionally, boundary layer transition strips of zig-zag shape and 0.05 mm height were used to emulate the full-scale boundary layer and prevent separation bubbles on the leading edge (LE) [12]. In principle, the chordwise position of strips and their thickness depends on the values of parameters such as Ω, λ and ξ [8], which were allowed to vary during the WT testing campaign. Since their relocation between runs would be impractical, they were positioned based on the guidelines of [12], at a fixed 5% chordwise position on the suction side (SS) and 30% on the pressure side (PS).

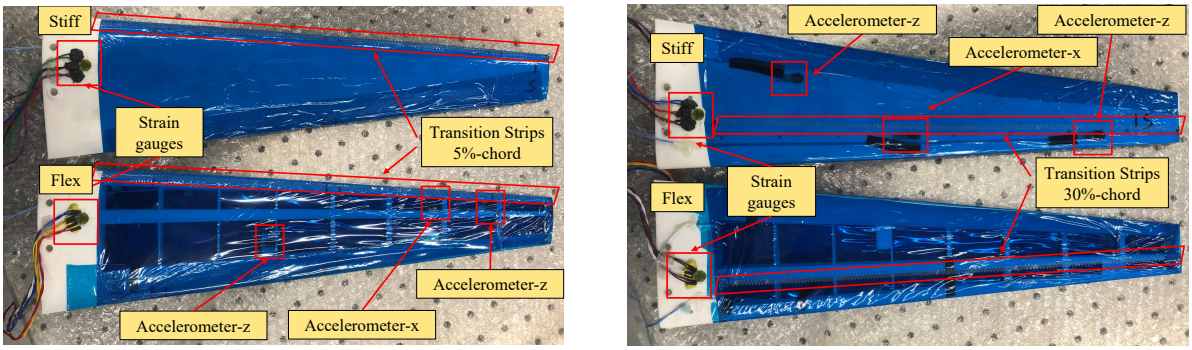

(a) Suction Side **(b) Pressure Side**

Fig. 3 Blades instrumentation

In terms of on-board instrumentation, both blades featured strain gauges and accelerometers. Starting with strain-gauges, two Kyowa KFGS-5-120-D17-23 triaxial stacked rosettes were integrated at the blade root, one on the PS and one on the SS. The rosettes were positioned such that the strain gauges were oriented at -45°, 0°and 45°with respect to the blade's axis y. The strain gauges were combined in pairs to form half-bridge circuits, chosen specifically to amplify their sensitivity to blade root bending moments M_x (0^o PS-SS) or torsion moments M_y ($\pm 45^o$ PS, $\pm 45^o$ SS) alone. This configuration is also insensitive to temperature and axial loads [13]. To facilitate integration, the detailed design was adapted to include flat regions near the root to ensure good adhesion. Since the region was expected to feature separated flow due to the high angles of attack, no further adaptations were made for cable routing to mitigate interference drag; therefore, the cables were routed around the trailing edge (TE).

The blades featured three PCB 352A24 uni-axial accelerometers, two oriented in the out-of-plane direction z on the LE and TE respectively, and one in the chordwise direction x. The z accelerometers capture flapwise bending and torsion when used in tandem; placing them close to the blade tip ensures the best signal resolution as well as sensitivity to all vibration modes. However, given the small dimensions of tapered blades on the trailing edge region near the tip, there was limited space for a tandem placement (Fig.3). It was therefore decided to position the forward accelerometer as close as possible to the tip and the aft one at a spanwise position closer to the root, making sure to avoid the node of the second flapwise bending mode. The x accelerometer was placed closer to the tip, with the purpose of capturing edgewise vibration. The two designs were adapted to enable accelerometer integration by means of different auxiliary features, as seen in Fig.3. The flexible blades included flat regions next to the ribs, on which the sensors were glued, while cable routing was enabled by small notches at the juncture between the ribs and the leading and trailing edge beams. The stiff blades featured pockets on the pressure side, where the sensors were enclosed, as well as grooves for cable routing. In both cases, the application of the Oralight foil secured the cables into position and kept the aerodynamic shape in regions with no structural elements.

Additional adaptations were made on the blade root, to attach the blades to the aluminium hub, which encases the delta-3 hinge oriented at $\delta_3 = 63.5^o$ angle, as seen in Fig.4b. This was realised by means of joining plates, consisting of a flat plate and two inserts, as shown in Fig.4a. Three pairs of joining plates were produced, each corresponding to a different pitch setting (-2^o, 0^o, $+2^o$). This was achieved by changing the orientation of inserts relative to the flat plate accordingly. This solution proved to be sensitive to geometric tolerances, especially in the case of the inserts, where loose fits were found to be a source of free-play. The decision to 3D-print these parts compromised the quality of the fit, therefore the authors recommend higher precision manufacturing methods for these critical components. Similar to

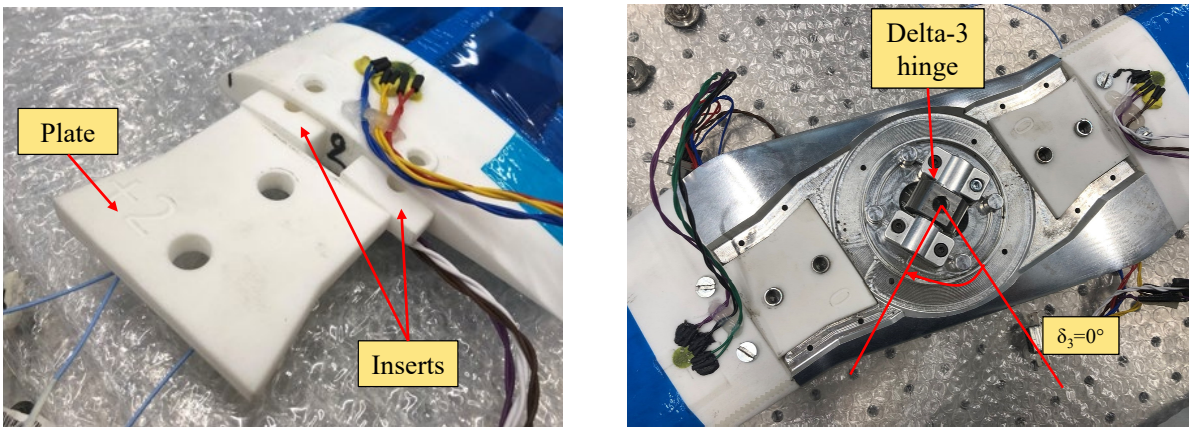

(a) Joining plate **(b) Hub**

Fig. 4 Rotor assembly

cable routing, given the expectation for separated flow due to the high angle of attack near the hub, the blades were simply joined using bolts, favouring practicality at the expense of additional drag near the blade root. It should be noted that all aforementioned adaptations were not accounted for in the FEM, assuming their effect to be negligible.

B. Test Rig

The rotor described in Section III.A was connected through the hub to the shaft of the test rig. Overall, the tower was oriented normal to the rotor plane, as shown in Fig.5. The test rig was firmly connected at its bottom to the OJF balance, which was in turn secured on a movable platform. The platform's height was adjusted according to the ξ angle in order for the rotor to remain in the center of the wind tunnel flow and avoid the region beyond the boundary streamline of the jet [14]. The tower was allowed to rotate with respect to a pivot point on the base of the rig. This feature allowed testing at different ξ. Dynamic tilting was outside the scope of this study, so the tower orientation was fixed during runs.

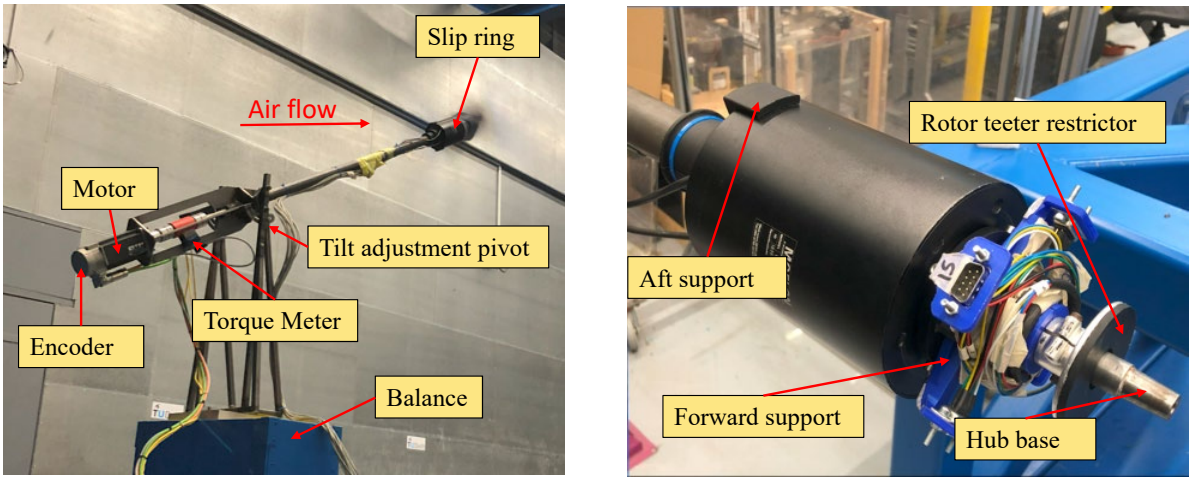

(a) Main components **(b) Slip ring configuration**

Fig. 5 Test rig

The top end of the tower featured a GT50119-S30 slip ring, as seen in Fig.5, with the purpose of signal transmission from the onboard sensors to the Siemens SCADAS Mobile data acquisition (DAQ) system in the stationary reference frame. The slip ring was integrated in the tower by means of two 3D-printed supports, shown in Fig.5b. The aft support (black) connected the shaft casing to the slip ring's stator. Likewise, the shaft and slip ring rotor were connected through

the forward support (blue). The forward support also served as a base for the 9-pin connectors, ensuring orderly cable routing. Tight tolerancing was found necessary to avoid unstable oscillations due to mass eccentricity. Finally, a rotor teeter restrictor was placed between the hub and the aforementioned equipment to avoid damage in the event of high amplitude oscillation; such unstable dynamics could be provoked by operation in stall, as proposed by Krishnan et al. [10].

Some more instruments were placed at the bottom end of the tower, shown in Fig. 5a. Rotational speed was controlled by a Unimotor hd 067 servomotor, at the rear end of the shaft. Torque was measured using a DATAFLEX®16/10 torque meter. Finally, a CFS50 encoder was also included, producing a pulse signal each time the rotor crossed the reference azimuthal position.

Three DAQ systems were used to record the experimental data. Twelve channels of SCADAS were used to collect the signal from blades (six uni-axial accelerometers, six half-bridge strain sensors). The OJF balance measured three forces and three moments acting at the base of the rig and transmitted their signals through six channels to the OJF DAQ. Finally, the signals from the torque meter, servomotor and encoder were collected using a custom LabVIEW recording application. The encoder's signal was also transmitted to a SCADAS channel to permit the synchronization between blades' and rig's data. Most importantly, it allowed the correlation of blade acceleration and strain data with the rotor's azimuthal position ϕ. The azimuthal position of blade 1 is aligned with that of the rotor; the position of blade 2 has a 180^o offset.

IV. Ground Testing

Ground testing preceded the WT tests with the aim of calibrating the strain gauges as well as evaluating the previously developed FE model for the rotor's static and dynamic responses.

A. Static Test

Static load testing serves two purposes: the calibration of the strain-gauges and the measurement of their corresponding deformed shapes. A single testing campaign is normally sufficient, using cases of pure bending and pure torsion applied at the blade tip. Due to the lack of equipment availability for the measurement of deformed shapes combined with the need to monitor blade root loads during the WT testing campaign, static testing was split into two sessions, each focusing on one of the two aforementioned goals.

Load application was made possible through the use of clamps applied at the spanwise locations of the 3^{rd}, 6^{th} and 9^{th} rib; this ensured firm contact conditions between the blades and the clamps. The clamps featured hooks at three chordwise positions: leading edge, blade elastic axis and trailing edge, allowing the application of pure bending/torsion or mixed load cases. The test matrices were tailored to the objectives of the respective testing sessions, however both sessions featured clamped boundary conditions, enforced by firmly securing the quasi-rigid aluminium hub on a workbench. The two test set ups are compared in Fig.6, showing the calibration test setup under a pure bending case in Fig.6a and the shape measurement setup under a pure torsion case in Fig.6b; in the latter a pulley system was introduced to enable torsion loads by means of a force couple.

1. Strain Gauge Calibration

The session dedicated to strain gauge calibration featured three training load cases, as well as, two validation load cases. The training load cases were chosen to be linearly independent and to generate large M_x,M_y at the blade root, yielding a high signal-to-noise ratio. Specifically, increasing loads were incrementally applied at the LE and TE x-positions of the 1^{st} clamp (mixed load) as well as the blade elastic axis position (MID) of the 3^{rd} clamp (pure bending); this was repeated for the blades in both upside up and down positions. Viscoelastic hysteresis caused a constant strain offset between cases of equal load during loading and unloading. Being mainly interested in the linear elastic response, the raw voltage readings were normalised with respect to the corresponding zero-load readings, which were non-zero due to the influence of gravity and a constant offset due to small deviations in resistance. As seen in Fig.7 each sensor responds differently to each load case, however a linear fit can be observed. Due to the use of mixed load cases, the number of load increments are shown on the x-axis, instead of M_x and M_y. Additional notable observations include the relatively large magnitude of the measured voltage for the strain-gauges oriented at 0°, as well as the non-zero sensitivity of the ±45°sensors to pure bending (especially in the SS strain gauges), possibly due to the imperfect alignment of the strain rosette with the blade's elastic axis .

For each of the four blades, a linear operator was calculated, relating the sensor voltages to the loads. The operators

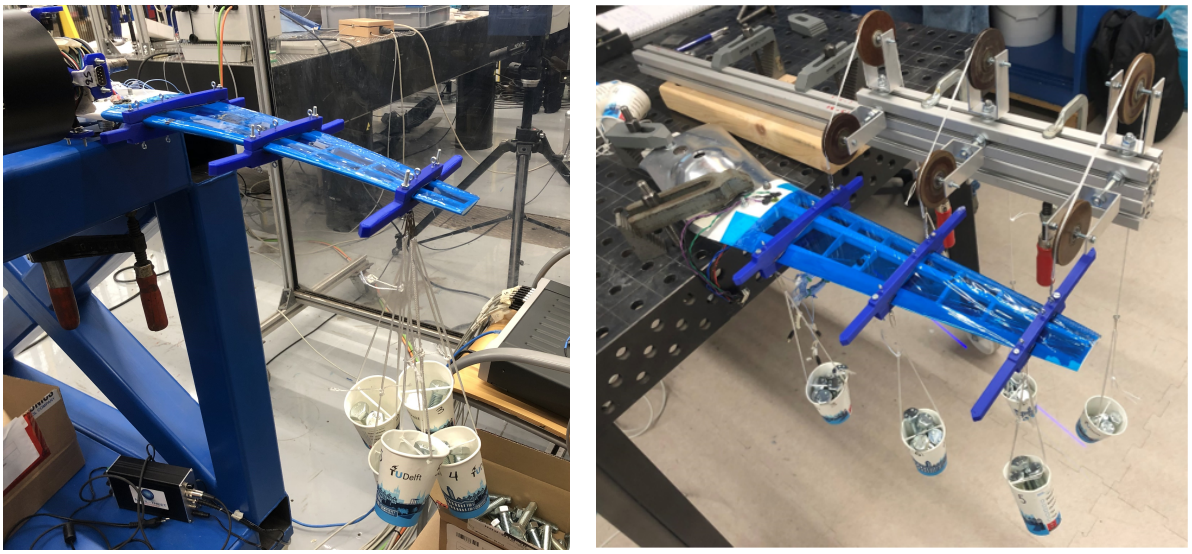

(a) Strain gauge calibration, pure bending **(b) Deformed shape measurement, pure torsion**

Fig. 6 Static test configurations

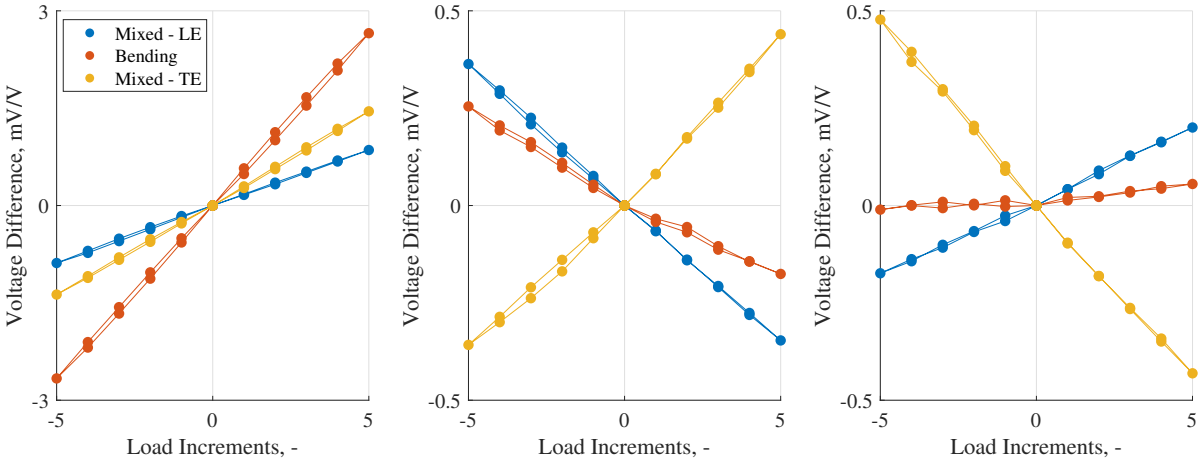

(a) 0° **(b) ±45°suction side** **(c) ±45°pressure side**

Fig. 7 Strain sensor calibration readings (Flexible blade)

were calculated by means of linear least squares regression. Upon calculating these operators, the accuracy of the strain-based load reconstruction can be assessed using two mixed load validation cases, featuring loads along the LE and TE respectively, ensuring linear independence from the training load cases. The results are presented in Table1, where the M_x was consistently calculated within 4.5% error whereas the error in the calculation of M_y was larger (28%), as expected due to its relatively lower magnitude. This result indicates that M_y will be poorly resolved in the presence of significantly larger M_x.

2. Deformed Shape Measurement

Deformed shape measurement provides insight into the stiffness distribution of the blade structure. More precisely, this data is used to test, first, the accuracy of FE model prediction of the structure's stiffness, second, the difference in stiffness between blades 1 and 2 of each set and third, the effect of different joining plates on the total displacement.

To answer the above questions, pure bending and torsion load cases were used, featuring loads along the full span of the blade, in order to induce strain across the entire structure; the experimental setup is presented in Fig. 6b. Bending

Table 1 Strain-based load reconstruction

		Leading edge		Trailing edge	
		$M_x[Nm]$	$M_y[Nm]$	$M_x[Nm]$	$M_y[Nm]$
Flexible	ref.	3.07	0.49	3.07	-1.19
	Blade 1	2.99 (-2.5%)	0.52 (+6.1%)	3.13 (+2.3%)	-1.14 (-4.2%)
	Blade 2	3.02 (-1.5%)	0.53 (+8.2%)	3.21 (+4.5%)	-1.20 (+0.9%)
Stiff	ref.	3.66	0.65	3.66	-1.56
	Blade 1	3.74 (+2.2%)	0.62 (-4.5%)	3.66 (-0.1%)	-1.41 (-9.5%)
	Blade 2	3.50 (-4.5%)	0.46 (-28.4%)	3.73 (+1.8%)	-1.58 (+1.0%)

cases featured a single shear force point load f_z at the tip. Instead, torsion point loads m_y were applied using force couples at three spanwise locations, so as to improve the signal-to-noise ratio. The deflected shapes were measured by means of 3D-scanning the upward-facing surface of the blade, with particular emphasis on the clamp protrusions, which featured "dimples" at the tips to be used as reference points; this was particularly useful for the calculation of twist, as pure torsion cases featured deflections of relatively smaller magnitude and this was another effective way to improve the signal-to-noise ratio of the raw data. Results from bending and torsion cases are focused on flapwise displacement Δz and torsional rotation $\Delta\theta$ respectively. In both cases the z-displacement of the dimples is consolidated into the Δz and $\Delta\theta$ of the blade axis.

In order to assess the quality of blade construction in terms of agreement with FEM and symmetry within blade pairs, blade 1 of the flexible and stiff pair was loaded incrementally in bending and torsion. The unit load increments are presented in Table 2. Starting from the unloaded case (L0), unit loads were added incrementally and then removed; a total of three load cases were tested (L1, L2, L3) along with the two unloaded cases. The initial unloaded shape is used as reference for the calculation of the deflected shapes. Measurements were made in both upward and downward facing orientations. In the interest of brevity, blade 2 of each pair was only tested facing downwards at full bending and torsion load. All the above test cases were performed using the same joining plate corresponding to a 0^o pitch setting. The deflected shapes from the downward facing load cases are compared to numerical predictions in Fig. 8 and 9 for flexible and stiff blades respectively. The experimental data are presented in terms of blade number (B1, B2), whether loads were being added (ON) or removed (OFF) and the loading step. The shapes predicted by FEM are also included for reference, each of the three curves corresponding to the respective load case. Results from the upwards facing cases are omitted as they exhibit the same trends, adding little to the discussion.

Table 2 Unit load increments

		Span. pos.	Bending Case		Torsion Case	
		$y[m]$	$f_z[N]$	$m_y[Nm]$	$f_z[N]$	$m_y[Nm]$
Flexible	Clamp 1	0.227	0	0	0	0.193
	Clamp 2	0.387	0	0	0	0.139
	Clamp 3	0.547	2.501	0	0	0.044
Stiff	Clamp 1	0.227	0	0	0	0.290
	Clamp 2	0.387	0	0	0	0.139
	Clamp 3	0.547	4.169	0	0	0.044

An additional set of measurements was performed to assess the effect of joining plates on displacement, focused on blade 1 of the flexible blade pair in the downwards facing orientation. Five more joining plates were used, collecting data for all pairs of plates (-2^o, 0^o, $+2^o$) used in the WT tests. Results for the fully loaded bending and torsion cases are presented in Fig. 10. To facilitate modelling, in FEM the blades are fully attached to the hub; given the hub's relatively high stiffness, this effectively corresponds to clamped boundary conditions. In reality, the joint was found to act as a rotational spring, imparting displacement due to rotation, which propagates along the span. Ultimately, the measured Δz is the sum of the elastic deformation Δz_{el} and the component due to rotation Δz_{rot}. Assuming that the

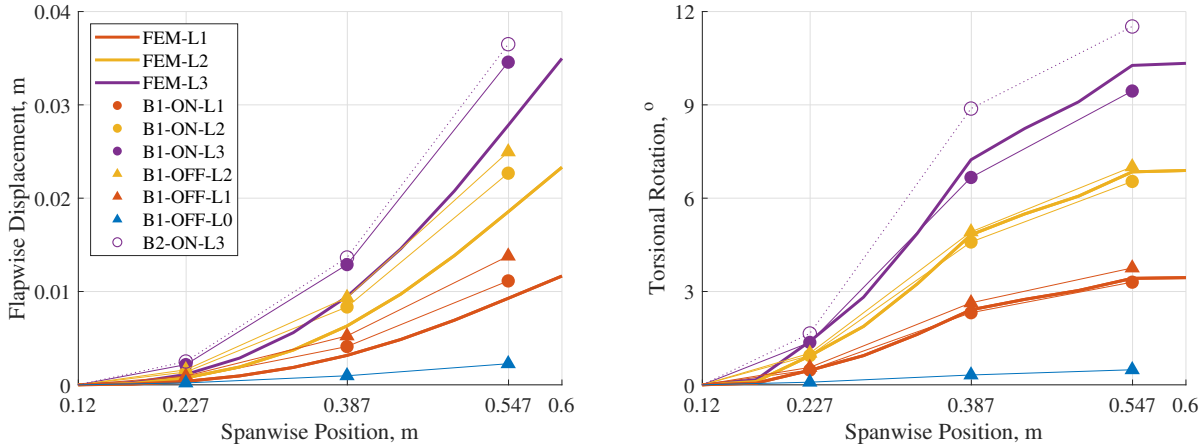

(a) Pure bending case **(b) Pure torsion case**

Fig. 8 Deformed static shapes - flexible blades

former is common between runs, the latter can be extracted. The measured shapes are presented in Fig. 10a, along with the "corrected" shape, featuring only Δz_{el}. The same principle holds for twist under torsion, where a constant offset rotation originating at the blade root would be expected. However, due to the increased sensitivity of these results to measurement error, as well as increased stiffness of the joint in torsion, this effect was not measured and is therefore not presented in Fig. 10b.

With regards to modelling accuracy, both blade pairs were found to be more flexible in bending than predicted, by 14% and 31% for flexible and stiff blades respectively. Upon correcting for Δz_{rot}, this mismatch is reduced, as seen in Fig. 10a for the flexible blades. Still, the FEM blades are stiffer, possibly due to inaccurate modelling of the effect of the film skin. This hypothesis is further supported by the greater difference in $\Delta\theta$ between flexible blades 1 and 2. This is not the case for Δz which is dictated by the 3D-printed chassis, ultimately resulting to symmetric bending stiffness. The mismatch in stiffness appears more severe for the stiff blades, however it should be noted that the effect of Δz_{rot} is relatively larger in this case, since a given load case would result in less Δz_{el} but the same Δz_{rot}. Unlike flexible blades, in the absence of data using multiple joining plates, it is not possible to isolate the elastic component and further comment on the model's predictive ability. A better match is observed for both blade pairs in torsion, where the effects

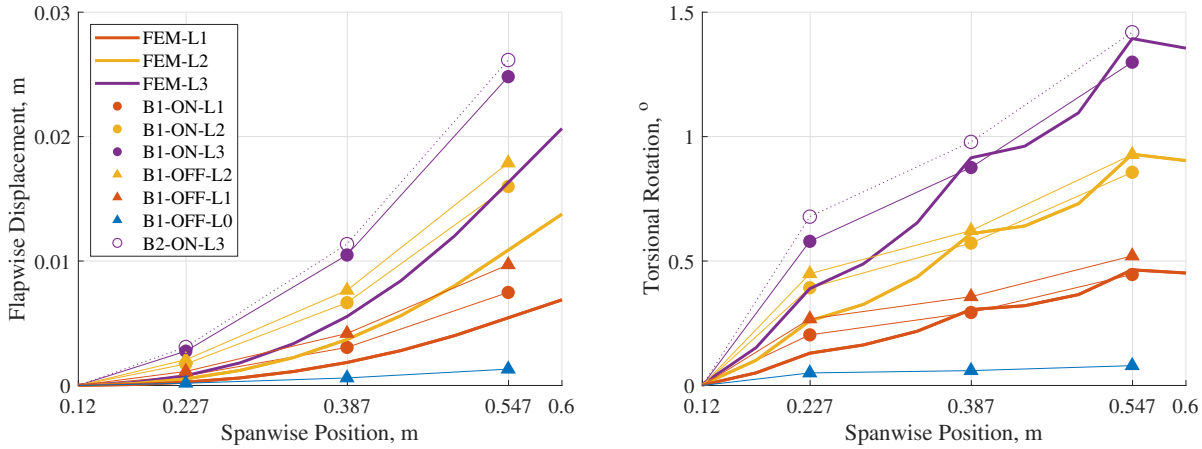

(a) Pure bending case **(b) Pure torsion case**

Fig. 9 Deformed static shapes - stiff blades

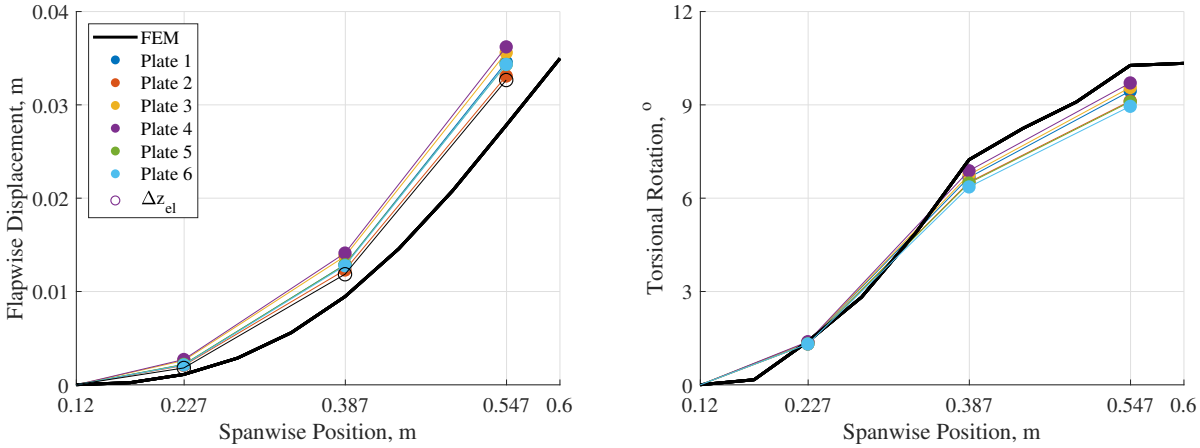

(a) Pure bending case **(b) Pure torsion case**

Fig. 10 Deformed static shapes - flexible blades, variable joining plates

of the joining plate are less pronounced, especially in the flexible blade pair, which exhibits relatively large twist. In the stiff blades, a small offset can be observed in the experimental data, possibly due to the joining plate's rotation.

Another important observation can be made by comparing deflected shapes corresponding to the same load case during loading and unloading. Significant hysteresis is observed in both blade pairs for both bending and torsion. This can possibly be attributed to the viscoelastic nature of the blade material, as noted in the strain-gauge calibration section; such nonlinear material properties were not considered in the FEM, where the structure was modelled as linear elastic to facilitate calculations. Alternative sources of hysteresis also include loose connections at the joints. In conjunction with the above discussion, it is evident that the effect of the joints on blade stiffness is significant and was modelled inadequately. The modelling approach proposed by Georgopoulos et al. [11] would need to account for these features, to improve FEM accuracy. In addition, local design adaptations are recommended, to impart tighter tolerances. These adaptations would mitigate errors in bending predictions.

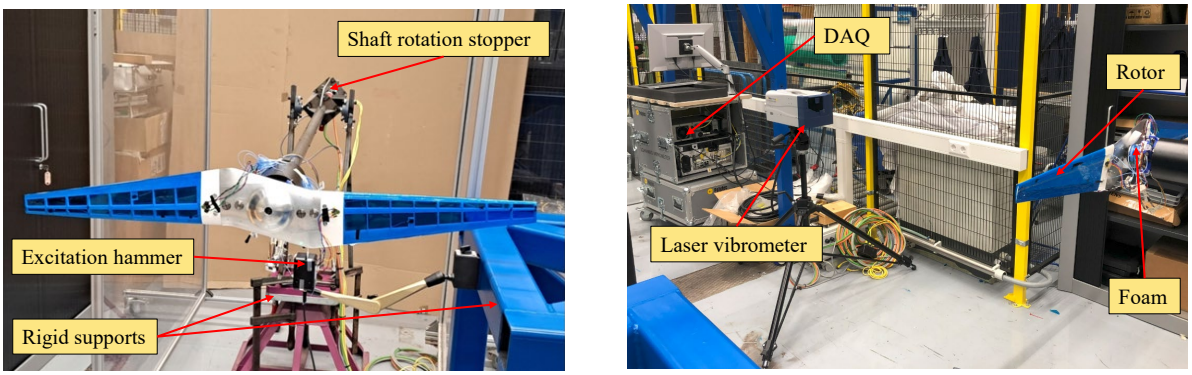

(a) Supports and excitation **(b) Measurement equipment**

Fig. 11 Ground vibration test configuration

B. Ground Vibration Test

The ground vibration test (GVT) was necessary to validate that the structural dynamic behavior of the constructed model was close enough to FEM predictions. Even though the FEM only accounted for the rotor's structure, it was decided to conduct the GVT with the rotor attached to the test rig, to reveal potential dynamic coupling between the rotor and the rig. Therefore, the rig's base was fixed at the bottom and the shaft was constrained by a clamp at the bottom of

the tower, as can be seen in Fig.11a. Moreover, soft foam was placed between the rotor teeter restrictor (Fig.11b) and the hub. The intention was to approximate a free hinge condition [15] whilst keeping the rotor in a stationary vertical position, ensuring straight, reversible hammer hits. The stiffness of the foam was not calculated, however it was assumed to be low enough to not affect the rotor's antisymmetric vibration modes.

Table 3 Numerical and measured modal frequencies

Blade	Mode	Frequency (Hz)		Difference(%)
		FE	GVT	
Flexible	1st Flapwise Symmetric	18.6	18.7	0.5
	1st Flapwise Antisymmetric	25.4	30	18.1
	2nd Flapwise Symmetric	70.8	69.1	-2.4
	2nd Flapwise Antisymmetric	84.3	75.3	-10.7
Stiff	1st Flapwise Symmetric	24.3	21.0	-13.4
	1st Flapwise Antisymmetric	36.9	30.2	-18.2
	2nd Flapwise Symmetric	79.9	73.0	-8.6

The comparison between the FEM predictions and the measured modal frequencies is presented in Table 3 for a range of 0 to 100Hz; only the well resolved modes are presented. There are differences up to 18.2%, possibly attributed to a combination of inadequate modelling approaches and manufacturing imperfections, as discussed in the preceding sections. A hinge rigid body mode (HRB) was also measured at 17.8 Hz using both flexible and stiff blades. It is therefore hypothesized that the foam used to enforce a "soft-spring" boundary condition was not appropriate. This is also expected to cause antisymmetric modes to appear stiffer, leading to higher natural frequencies.

V. Wind Tunnel Testing

A. Methodology

A WT testing campaign was executed in the OJF of TU Delft. The scope of the experiments was to investigate the rotor's aeroelastic response by means of a parametric sensitivity study. The following variables were considered: ξ = {60°, 30°}, Ω = {450, 600, 750 RPM} and β = {-2°, 0°, +2°}. Test runs were performed at λ = {3.5, 4, 5, 6, 8} using both developed blade pairs {flexible, stiff}. Runs at λ = 3 were also performed but are omitted from the sensitivity analysis, as the motor was not always able to maintain constant Ω, especially at 750RPM and ξ = 60°, possibly due to the high levels of torque on the shaft. Finally, some runs were performed with a constrained hinge, using the stiff blades. The conventions used for the above parameters are illustrated in Fig.12.

The configuration using the stiff blades at ξ = 60°, Ω = 600RPM and β = 0° was defined as the reference case relative to which the sensitivity analysis of Section V.C was carried out. Sensitivities are analysed for one parameter at a time, by comparing results to the reference case. In this context, blade type is treated as one more parameter, as observations made using the stiff blades with regards to the other parameters (ξ, Ω, β) also apply to the flexible blades.

The sensitivity analysis addresses the static and dynamic response using the respective quantities of interest. The former is captured by C_P, C_T and the static component of bending moment $M_{x,o}$. It was found that, despite connecting pairs of strain gauges in a half-bridge configuration, the $M_{x,o}$ signal was corrupted by temperature and/or axial stresses due to centrifugal loads. Therefore, the presented results are normalised with respect to the reference case corresponding to the given test run. The above sources of error are specific to each blade at each tested Ω value. The effects of gravity are also removed by accounting for ξ. Therefore, reference cases are defined using the λ = 8 run, for each blade and ξ, Ω value. The same reference case is used for variable β and hinge setting, which are assumed to not affect the error signal.

$$M_{x,ref} = \frac{1}{2}\rho V_{rel}^2(\pi R^2)R = \frac{1}{2}\rho(V_{rot}^2 + V_\infty^2)(\pi R^2)R = \frac{1}{2}\rho\left(V_{rot}^2 + \frac{V_{rot}^2}{\lambda^2}\right)(\pi R^2)R = \frac{1}{2}\rho(\Omega R)^2\left(\frac{\lambda^2+1}{\lambda^2}\right)(\pi R^2)R \quad (1)$$

The dynamic response is analysed in terms of the periodic component of bending moment $M_{x,p}$. The three quantities of interest include magnitude, azimuthal variation and harmonic content. The first two are captured using polar plots of

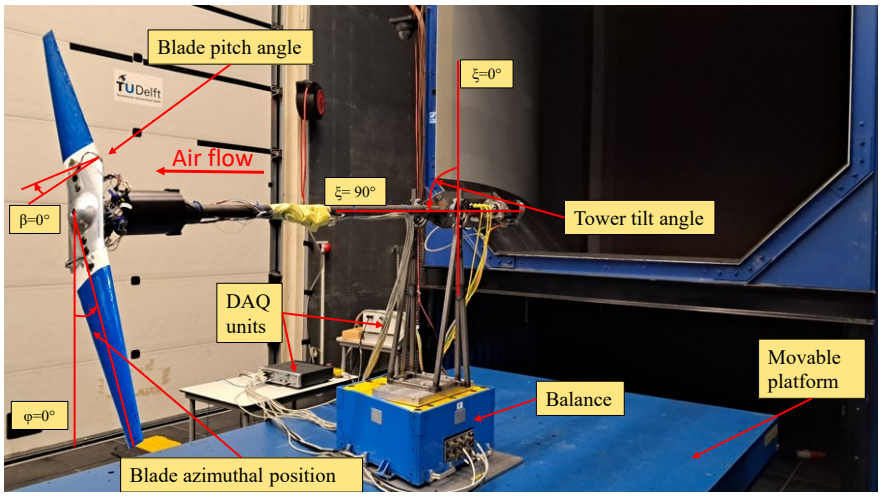

Fig. 12 Wind tunnel test configuration

the azimuthal variation of $M_{x,p}$, for each tested value of λ. The latter is presented in terms of the magnitude of the 1P, 2P and 3P harmonics in bar charts under the corresponding value of λ. Both $M_{x,o}$ and $M_{x,p}$ are made dimensionless by normalising with respect to the reference bending moment $M_{x,ref}$, as seen in Eq. (1). The effects of dynamic pressure on forcing magnitude are therefore removed, facilitating the comparison of the response among different Ω and λ cases.

B. Physical System Description

As presented by Georgopoulos et al. [11], the EoM for the wind turbine rotor capture the interaction among structures, rotordynamics and aerodynamics, as shown in Eq. (2), expressed in the rotational frame of reference.

$$[M_S]\ddot{\vec{x}} + [B_{CO}]\dot{\vec{x}} + ((1 + i2\zeta)[K_S] + [K_{CE}] + [K_{GE}])\,\vec{x} = \vec{f_A} + \vec{f_{CE}} + \vec{f_{GR}} \tag{2}$$

- Structure: structural mass $[M_S]$, structural stiffness $[K_S]$, structural damping ζ
- Rotordynamics: Coriolis damping $[B_{CO}]$, centrifugal stiffness $[K_{CE}]$, geometric stiffness $[K_{GE}]$, centrifugal force $\vec{f_{CE}}$
- Aerodynamics: aerodynamic load $\vec{f_A}$
- Gravity: gravitational force $\vec{f_{GR}}$

The EOM features linear rotordynamic stiffness and damping terms, which are coupled with the structural terms. In aircraft wing aeroelasticity, it is customary to obtain linear aerodynamic stiffness, damping and mass terms, derived from thin airfoil theory, to be coupled with the structural terms, yielding a monolithic expression for the EoM [16]. However, wind turbine blade aerodynamics are dictated by the induced velocity components, which reflect the thrust generated by the rotor. As a result, changes in displacement $\vec{x}$ and its derivatives have an impact on the flow field, affecting the velocity components on blade segments and hence the dynamic pressure and the angle of attack. Ultimately, there exists a coupled, non-linear relation between blade kinematics and the aerodynamic loads. The system is therefore treated as a rotating structure under external loading. The aerodynamics, as dictated by the rotor's azimuthal position ϕ, blade kinematics and induced velocity components, are treated as a periodic external load.

Therefore, the aerodynamic loads can be decomposed into three terms: the constant load $\vec{f_{A,o}}$, the random excitation due to turbulence $\vec{f_{A,t}}$ and the periodic aerodynamic load $\vec{f_{A,p}}$. Accordingly, the response of the system is made up of the corresponding components, which can be addressed individually. The effects of $\vec{f_{A,o}}$ are captured by C_P and C_T, while its effect on the structure is reflected by $M_{x,o}$, which corresponds to the static deformation $\vec{x_o}$. Turbulence leads to low amplitude vibration $\vec{x_t}$ of continuous frequency band, which was captured by the onboard accelerometers, at low power spectral density (PSD).

The third load component stems from the yaw angle γ between the rotor and the incoming flow, which gives rise to two phenomena. The lift dissymmetry due to the advancing-retreating blade aerodynamics[10] and the skewed wake effect [17] that causes variation of induced velocities with ϕ [18]. The former dominates the flow at low λ, with

maximum dissymmetry when the blades are at $\phi = 90^o$ and 270^o. The latter is more pronounced at higher λ, leading to maximum dissymmetry at $\phi = 0^o$ and 180^o. The pertinent aerodynamics are described in further detail by Krishnan et al. [10]. Given the rotor's downwind placement, the tower wake also introduces lift imbalance in the form of a negative gust at $\phi = 0^o$. Overall, the rotor experiences periodic aerodynamic loads and in turn a periodic response $\vec{x_p}$. Under steady-state operation, the same loads and response take place within a given cycle. Therefore, both can be treated as a Fourier series of fundamental frequency equal to Ω. The three response components can be seen in Fig.13. The static and periodic response are presented in the azimuthal variation of M_x, as seen in Fig.13a. In turn, a Fourier transform of blade tip acceleration a_{zt} reveals the continuous-frequency $\vec{x_t}$ along with the dominant discrete-frequency $\vec{x_p}$ at the rotational speed harmonics, shown in Fig. 13b.

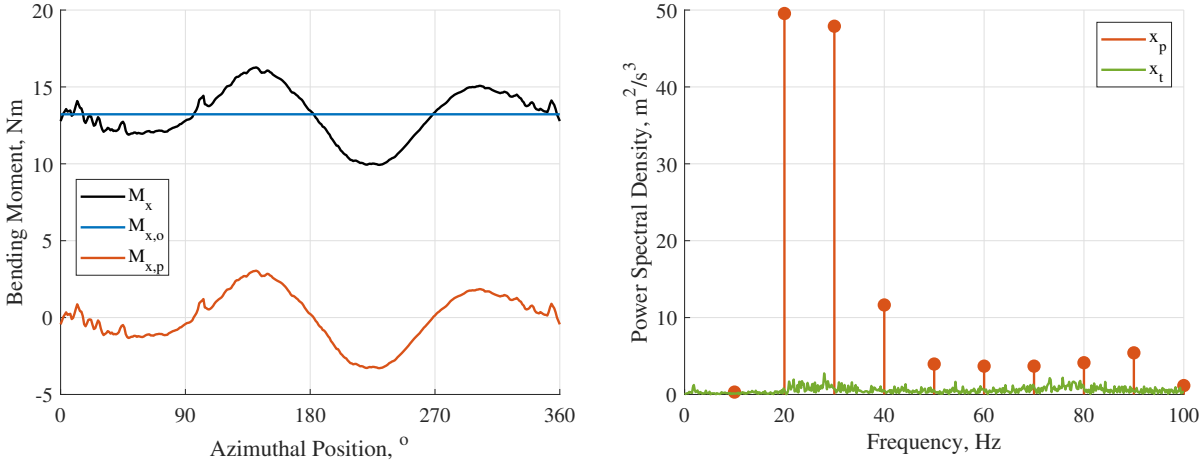

(a) Bending moment - azimuthal variation **(b) Acceleration - power spectral density**

Fig. 13 The three components of the response at $\xi = 60^o$, $\Omega = 600RPM$, $\beta = 0^o$, $\lambda = 3.5$ with flexible blades rotor

The above discussion motivates approaching the system as a structure under forced vibration, excited by the harmonics of the periodic aerodynamic load. Therefore, $\vec{x_p}$ is given by the superposition of modal responses to the harmonics. It is important to note that the system is assumed to be axisymmetric. This implies that the two blades experience identical periodic loads and exhibit an identical periodic response with 180^o offset from each other. Regarding the mode shapes, they are split into symmetric and antisymmetric, as discussed in Section IV.B. Given the condition of axisymmetry, odd harmonics (1P, 3P, 5P, . . .) exert opposite loads on the blades at a given instant, while the inverse holds for even harmonics (2P, 4P, 6P, . . .). By definition, the modal force given by the dot product of the mode shape and the applied force, is zero for symmetric modes excited by odd harmonics and antisymmetric modes excited by even harmonics.

$$\begin{aligned}\vec{x_p} = [q_{HRB}(\Omega)cos(\Omega t + \tau_{HRB}(\Omega)) + q_{HRB}(3\Omega)cos(3\Omega t + \tau_{HRB}(3\Omega))]v_{\vec{HRB}} \\ +q_{F1S}(2\Omega)cos(2\Omega t + \tau_{F1S}(2\Omega))v_{\vec{F1S}} \\ +[q_{F1A}(\Omega)cos(\Omega t + \tau_{F1A}(\Omega)) + q_{F1A}(3\Omega)cos(3\Omega t + \tau_{F1A}(3\Omega))]v_{\vec{F1A}}\end{aligned} \tag{3}$$

Consequently, the system can be decomposed into two parallel subsystems, consisting of the symmetric and antisymmetric modes and excited by even and odd harmonics respectively. Upon observation of experimental data, M_x is characterised by the $M_{x,o}$ and the first three harmonics of $M_{x,p}$; higher harmonics are occasionally observed in acceleration data, particularly in the vicinity of the 2nd flapwise modes (75.3 Hz for flexible and 73 Hz for stiff blades), but not in $M_{x,p}$. Also, low levels of edgewise mode excitation were detected and will therefore not be further considered. Therefore, $\vec{x_p}$ can be reconstructed as the superposition of the response of the HRB and 1st Flapwise Antisymmetric (F1A) modes to 1P and 3P forcing and the response of the 1st Flapwise Symmetric (F1S) mode to 2P forcing. From geometric stiffness, the HRB mode's natural frequency is equal to the rotational speed Ω and is mainly excited by 1P forcing. The elastic modes are excited in accordance to the proximity of their natural frequency to the forcing frequency.

The modal superposition yielding $\vec{x_p}$ is expressed in Eq. (3), where q is the amplification factor, τ is the phase, $\vec{v}$ is the mode shape and t is time. The effects of axisymmetry on the periodic response are presented in Fig 14. Figure 14a shows the acceleration of the two blade tips over a cycle whereas Fig. 14b and Fig. 14c show the magnitude and phase of the first 6 harmonics. As expected, the corresponding harmonics have roughly equal magnitude and equal (even harmonics) or opposite (odd harmonics) phase.

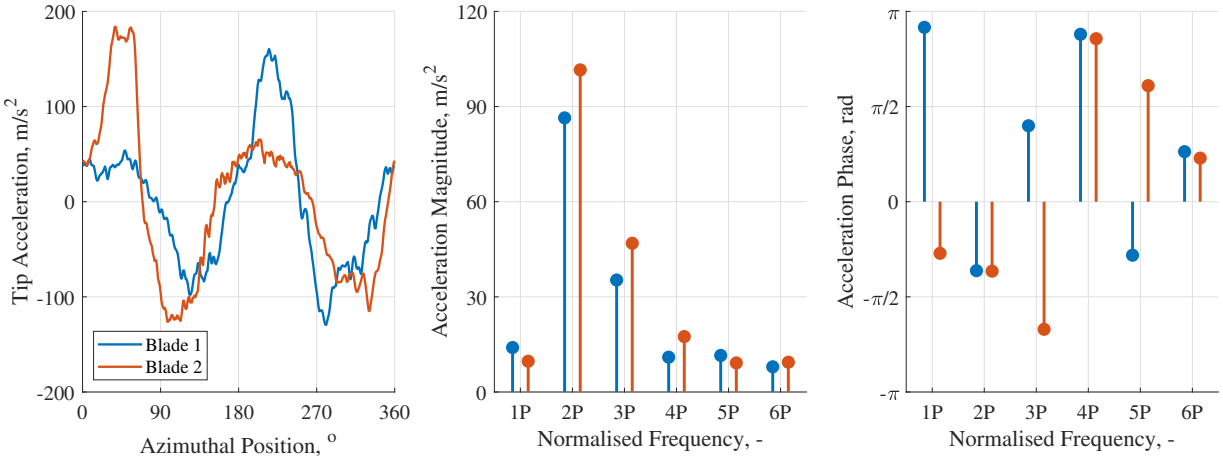

(a) Azimuthal variation **(b) Harmonics - Magnitude** **(c) Harmonics - Phase**

Fig. 14 Kinematic symmetry between the two flexible blades at $\xi = 30^o$, $\Omega = 600RPM$, $\beta = 0^o$ and $\lambda = 3$

Constraining hinge rotation ("fixed") and comparing the response relative to the unconstrained ("free") hinge configuration provides valuable insight into the system's functionality. This was achieved by placing the rotor teeter restrictor against the hub; in practice, this boundary condition was enforced imperfectly due to the rubber material at the point of contact, instead mimicking the effects of a rotational spring along the hinge axis. Nevertheless, hinge rigid body motion was significantly constrained. In terms of the modes, this has a profound effect on the anti-symmetric modes. In the low frequuency range, the HRB and F1A modes merge into a new 1st Flapwise Antisymmetric mode with fixed hinge (F1A$_{\text{fixed}}$). The F1A$_{\text{fixed}}$ has the same natural frequency as F1S and its mode shape exhibits antisymmetric blade deformation. The symmetric modes feature no hinge rotation and are therefore unaffected by this adaptation. Numerically calculated mode shapes of the stiff-blade rotor under 600RPM rotation are presented in Fig. 15 for the free hinge and Fig. 16 for the fixed hinge configurations. Despite the deviations revealed by the GVT, these results are indicative of the system's dynamics.

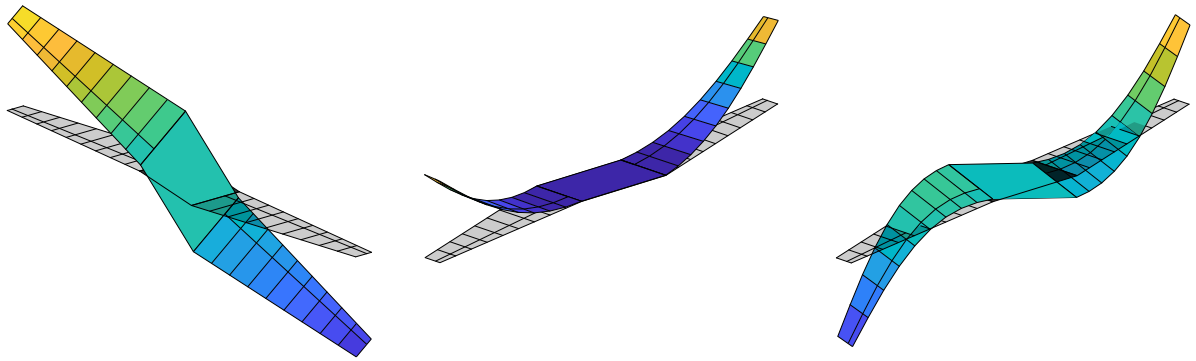

(a) Rigid Body mode **(b) 1st Flapwise Symmetric mode** **(c) 1st Flapwise Antisymmetric mode**

Fig. 15 Mode Shapes - Free hinge

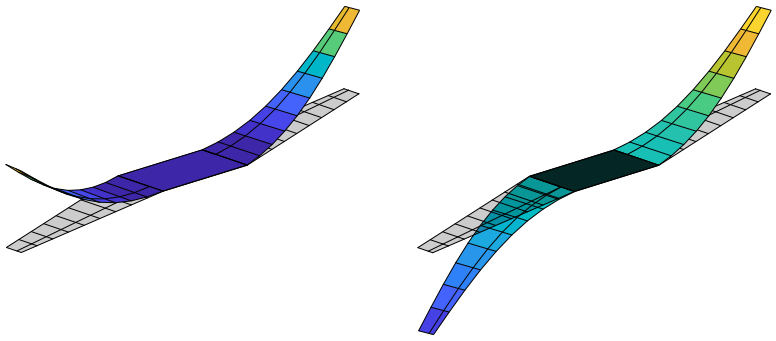

(a) 1st Flapwise Symmetric mode **(b) 1st Flapwise Antisymmetric mode**

Fig. 16 Mode Shapes - Fixed hinge

The response of the two hinge configurations is presented for $\lambda = \{3.5, 4, 5, 6, 8\}$, under the same operating conditions ($\xi = 60^o$, $\Omega = 600$RPM, $\beta = 0^o$) using the stiff-blade rotor. Fig. 17 is focused on the static response, in terms of C_P, C_T and $M_{x,o}$. The two configurations exhibit similar C_P-λ curves, both achieving maximum efficiency (free 22.9%, locked 21.3%) at $\lambda = 5$. However, the free rotor experienced higher static loads, as evidenced by the C_T-λ and $M_{x,o}$-λ curves.

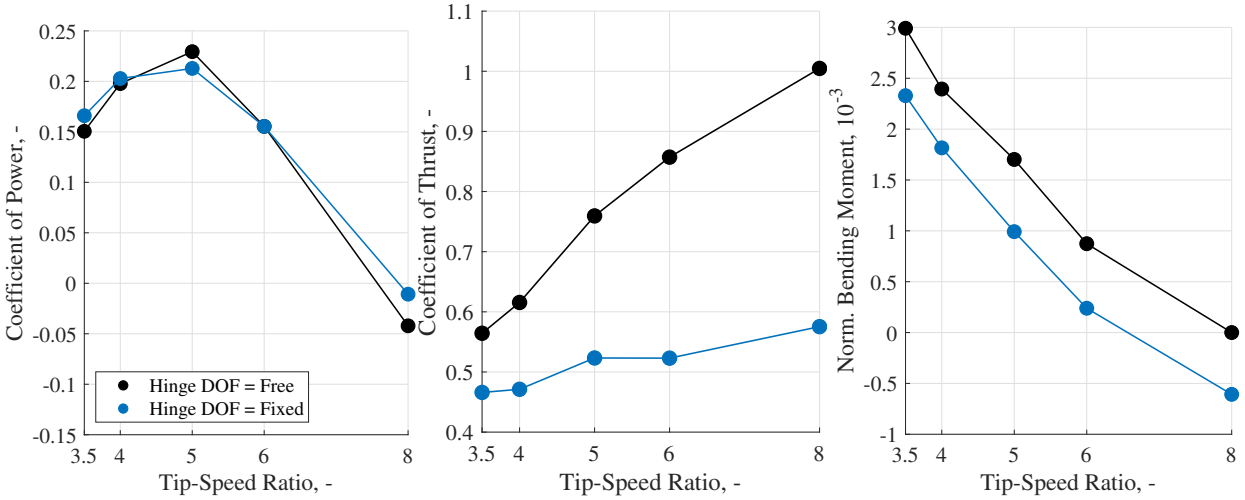

Fig. 17 Static response results, free vs fixed hinge at $\xi = 60^o$, $\Omega = 600RPM$ and $\beta = 0^o$ with stiff blades rotor

Figure 18 focuses on the periodic response. The variation of $M_{x,p}$ is plotted as measured on blade 1. In the fixed configuration, 1P loads dominate, accompanied by a smaller 2P component and a negligible 3P component, whereas 2P is the dominant frequency in the free condition for all λ. It is noteworthy that in the fixed-hinge case, the blade primarily deforms in the flapwise direction with a 1P frequency due to the uneven loading of the yawed rotor. This is caused by a combination of lift dissymmetry and the skewed wake and the inability of the rotor to teeter passively and balance the loads. Given the distance from the ($\text{F1A}_{\text{fixed}}$) natural frequency, the amplification $q_{F1A}(\Omega)$ is attributed to a large 1P forcing, rather than resonance.

In the free-hinge configuration, the HRB motion adds an extra degree of freedom to the system. When one blade faces a high lift condition at a certain azimuthal angle, ϕ, it moves upwards, contributing to a drop in its effective angle of attack by means of negative relative flapwise velocity and nose-down pitch, thereby reducing loads by 53% and 33% compared to the fixed-hinge case at $\lambda = 8$ and 3 respectively (Fig.18). Simultaneously, the other blade moves downwards, increasing its effective angle of attack. The hinge rotation continues until the loading on each blade becomes equal. As observed in Fig.18, there are two peaks in $M_{x,p}$ of almost equal magnitude in each rotation. In conjunction with

the effect of teetering motion on the induced velocity field, the above gives rise to a significant 2P forcing. Therefore, each blade experiences two ϕ regions with maximum positive loading and two with maximum negative loading in the free-hinge condition. Overall, the hinge motion acts to balance 1P loads, however inducing a significant 2P forcing component in the process; given its higher frequency, concerns are raised about quicker fatigue damage accumulation

Additional notable observations in Fig.18 include a dip of 60% in load magnitude at $\lambda = 5$ compared to $\lambda = 3.5$ for the free configuration. The dip in load magnitude aligns with the maximum C_P, suggesting a potential relation between blade kinematics and turbine efficiency that requires further investigation. If so, the $\lambda = 5$ condition could be targeted as the design operating condition with the added benefit of mitigating fatigue loads. Furthermore, a phase change of the $M_{x,p}$ profile is observed as λ decreases. This change is translated to 90° and 45° azimuthal rotation when 1P (fixed) and 2P (free) responses are dominant, respectively. This phase change is observed in both configurations and is attributed to the shift in the flow field, from the dominance of skewed-wake effects at $\lambda = 8$ to advancing-retreating blade lift dissymmetry at $\lambda = 3.5$

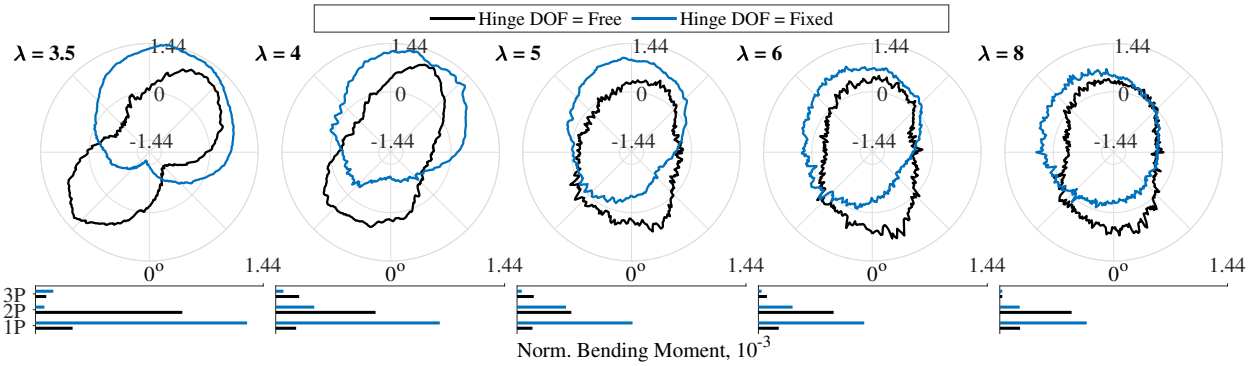

Fig. 18 Dynamic response results, free vs fixed hinge at $\xi = 60^o$, $\Omega = 600RPM$ and $\beta = 0^o$ with stiff blades rotor

C. Parametric Sensitivity Analysis

Having identified the fundamental characteristics of the rotor's static and dynamic response, this section delves into the sensitivity of the results concerning changes in system parameters, with the hinge consistently set to a free rotation with $\delta_3 = 63.5^o$. The conventions used in Section V.B are also used in this section. The examined parameters include blade type, ξ, Ω and β. Most observed sensitivities apply to both blade types, especially in the case of ξ and β variation. This is not the case for the dynamic response under variable Ω, therefore results from both blades are shown in Section V.C.3. The aforementioned reference case (stiff blades, $\xi = 60°$, $\Omega = 600$RPM, $\beta = 0°$) is always plotted (in black) to facilitate comparison among different sensitivity cases.

For brevity, accelerometer data are excluded from the sensitivity analysis. As previously mentioned, accelerometers capture responses to both $\vec{x_p}$ and $\vec{x_t}$. Regarding harmonic forcing, strain data sufficiently convey the quantities of interest related to $\vec{x_p}$. Since $\vec{x_p}$ predominantly consists of the first three harmonics of Ω, the accelerometers' sensitivity to higher harmonics would contribute minimally to the discussion. Concerning $\vec{x_t}$, no notable observations were made in response to parameter variations, as their magnitudes were very low compared to the values of the harmonics. It is worth noting that in cases with very low λ, turbulence excitation is high enough for $\vec{x_t}$ to be recorded by accelerometers (Fig.13b). In such instances, an amplification in the frequency band close to the elastic modes' natural frequencies was observed. However, this amplification was still significantly lower than the amplitude of the discrete periodic response. Ultimately, both the discrete periodic and the banded elastic mode responses were bounded, and no dynamic instabilities were observed in any of the test cases.

1. Blade type

The first parameter investigated for its influence on the rotor's aeroelastic response was the blade stiffness. Both flexible and stiff blade sets represented elastic structures, with the former aiming to capture the full-scale rotor's deformation and the latter its dynamic behavior. In terms of the static aeroelastic response, stiff blades exhibited higher C_P of nearly 21% across all λ range, except for cases with $\lambda = 4$ and 3.5, , where they exhibited values very close to those of flexible blades. Both blade sets showed similar C_T values in the mid-range of λ. The flexible set experienced

lower loading, particularly in low λ conditions, as indicated by $M_{x,o}$. There is a contrasting trend in the difference between the two blades in the C_P and $M_{x,o}$ graphs: at $\lambda = 3$, they displayed the maximum difference in $M_{x,o}$ but equal C_P, while at $\lambda = 8$ with C_P becoming negative, the inverse relationship held.

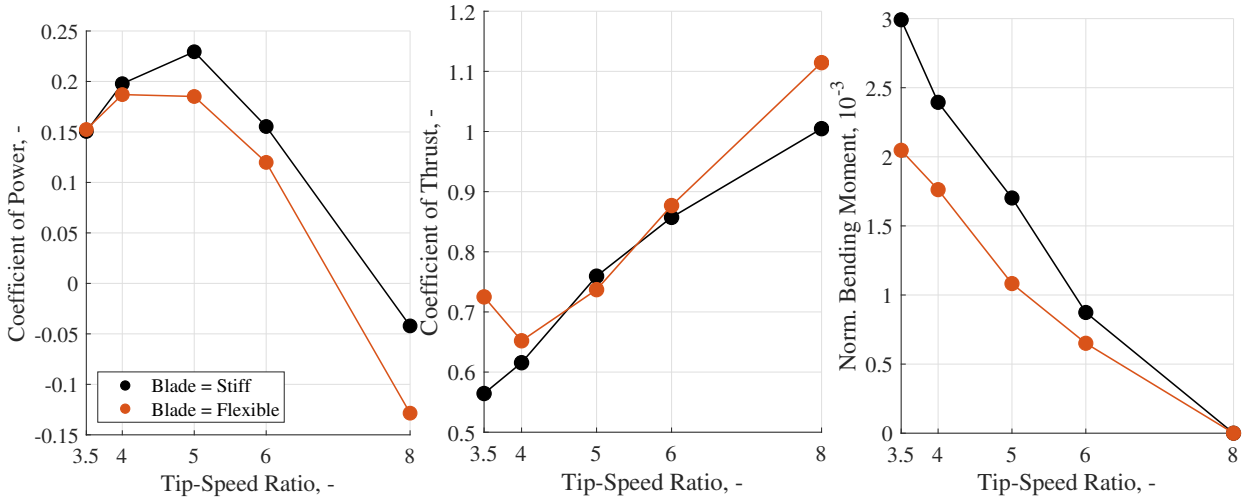

Fig. 19 Static response results, stiff vs flexible blades at $\xi = 60^o$, $\Omega = 600RPM$ and $\beta = 0^o$

Moving to the dynamic response, flexible blades demonstrated 70% lower $M_{x,p}$ at $\lambda < 5$ cases, compared to their stiff counterparts, potentially due to their higher magnitude of flapping. In an elastic structure, flapping induces a relative normal velocity component in the opposite direction of its motion, resulting in smaller effective angles of attack and, hence, lower loading. The above hypothesis does not take the effect of flapwise motion on induction values into account, calling for further investigation. Furthermore, the ϕ of maximum $M_{x,p}$ values varied consistently for both blades as λ decreased from 8 to 3.5. Notably, flexible blades exhibited a relatively higher 3P response (30Hz) compared to the corresponding harmonic of stiff blades, where a dominant 2P response (20Hz) was observed. This observation can be explored by considering that both blades' F1A modes have natural frequencies of nearly 30 Hz. This is not the case for F1S, where 21Hz and 18.7Hz was measured for stiff and flexible blades respectively (Table 3). Therefore, the 2P dominance in stiff blade's response could be attributed to its amplification by the F1S elastic mode, whereas the higher distance between 2P and F1S frequencies in flexible blades permits the 3P component's higher amplification.

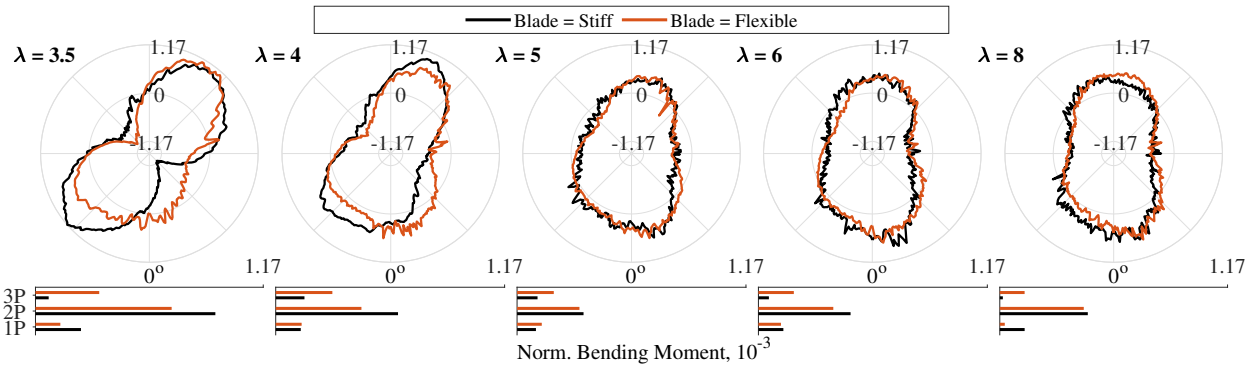

Fig. 20 Dynamic response results, stiff vs flexible blades at $\xi = 60^o$, $\Omega = 600RPM$ and $\beta = 0^o$

2. Tower Tilt Angle

Tilt angle, ξ, was found to have a crucial effect on the static aeroelastic response of the rotor. It is important to note that ξ defines the yaw angle of the rotor following the convention $\gamma = 90^o - \xi$. In all quantities of Fig.21 -C_P, C_T, and $M_{x,o}$- $\xi = 60^o$ exhibits higher values than the $\xi = 30^o$ case, as expected from previous studies demonstrating a reduction in C_P analogous to the cubic cosine of γ [19].

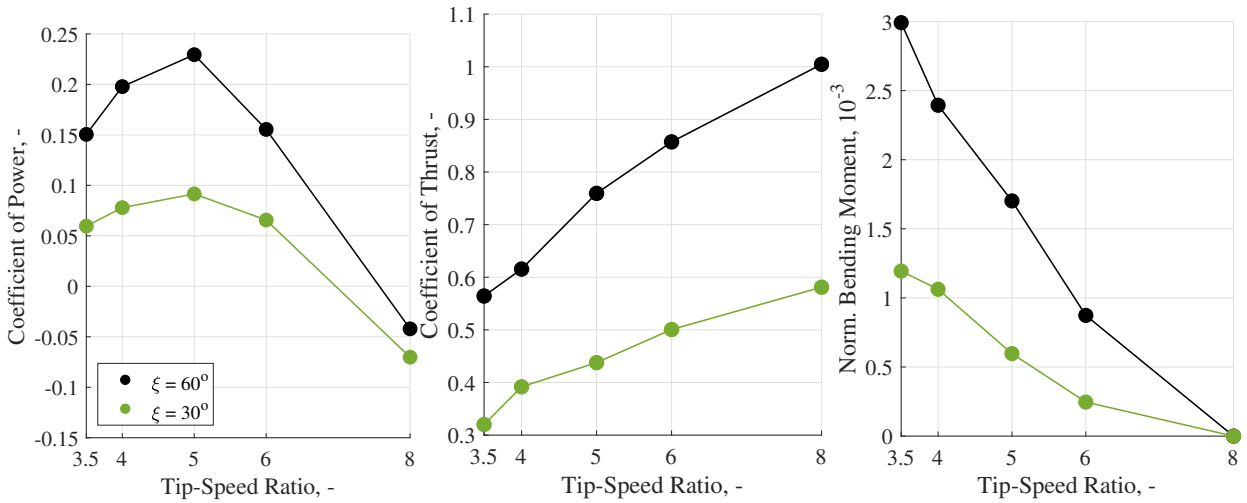

Fig. 21 Static response results, variable tower tilt angle at $\Omega = 600RPM$, $\beta = 0^o$ with stiff blades rotor

In contrast to the static response, $\xi = 30^o$ exhibits higher $M_{x,p}$ harmonics than $\xi = 60^o$ in Fig.22 ranging from 48% to 76%. This difference can be explained by the fact that both phenomena causing the periodic aerodynamic imbalance (lift dissymmetry and skewed wake) are enhanced by the increase in γ [18, 19]. The higher $M_{x,p}$ values of the $\xi = 30^o$ configuration are also represented by higher 2P and 3P components in the frequency domain. It is worth mentioning that the relative difference in the amplitude of 2P and 3P between the two cases is similar since both cases rotate at the same Ω and use stiff blades with the same elastic mode frequencies. Regarding the ϕ rotation of $M_{x,p}$ peaks with a reduction in λ, both tilt settings exhibit the same trend, with $\xi = 30^o$ rotating slightly more, probably due to a more extreme contrast between advancing-retreating blade aerodynamics ($\lambda = 3.5$) and the skewed-wake effect ($\lambda = 8$).

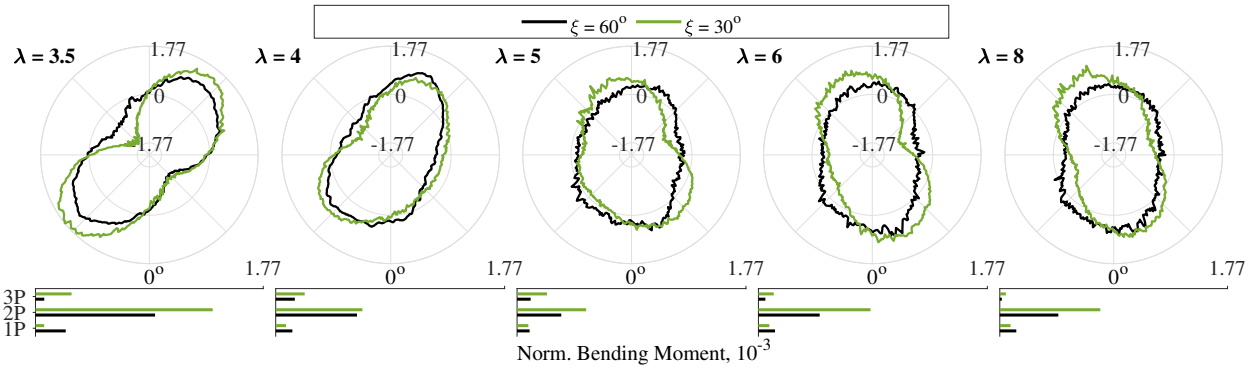

Fig. 22 Dynamic response results, variable tower tilt angle at $\Omega = 600RPM$, $\beta = 0^o$ with stiff blades rotor

3. Rotational Speed

The static aeroelastic response of the rotor exhibits negligible sensitivity to Ω. C_P remains at similar levels across all Ω values, as presented in Fig.23. Weak trends are observed in C_T and $M_{x,o}$, where $\Omega = 450$ RPM and $\Omega = 600$ RPM show the maximum levels, respectively. The elevated C_T value at $\Omega = 450$ RPM and $\lambda = 8$ could be attributed to low thrust in the numerator, which is susceptible to noise and poor calibration. Overall, no sensitivity is observed to Ω variation.

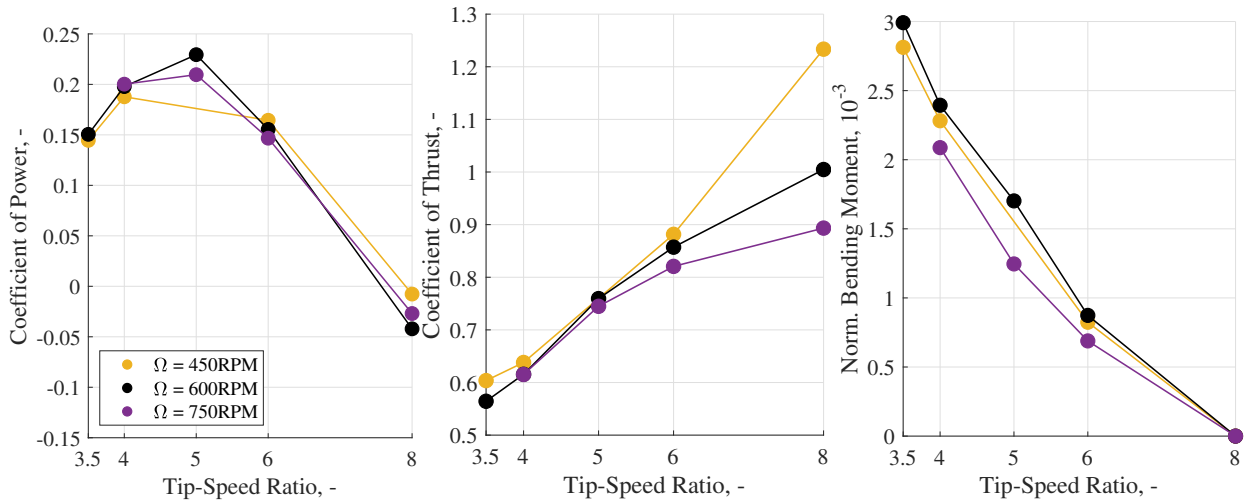

Fig. 23 Static response results, variable rotational speed at $\xi = 60^o$, $\beta = 0^o$ with stiff blades rotor

In contrast, the dynamic response is notably influenced by Ω. The normalization presented in Section V.A allows for the isolation of other parameters' influences, such as elastic mode amplification or variations in the induced velocity field. As depicted in Figure 24, at Ω = 750 RPM, $M_{x,p}$ experiences higher values compared to the other two conditions. Specifically, $M_{x,p}$ is 116% and 39% higher at Ω = 750 RPM compared to Ω = 600 RPM for $\lambda = 8$ and 4, respectively. Moreover, there is an approximately 45^o difference in the ϕ where peak values appear between the two rotational speeds, and this trend persists across all λ values.

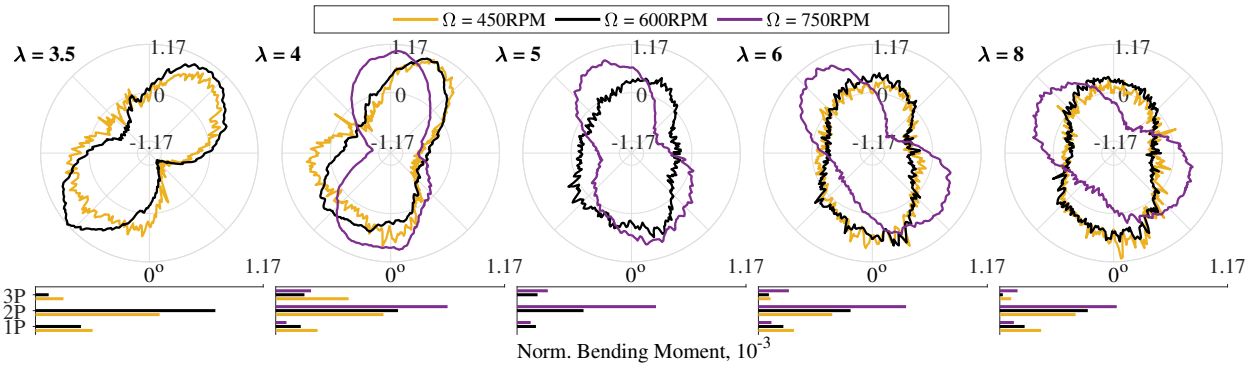

Fig. 24 Dynamic response results, variable rotational speed at $\xi = 60^o$, $\beta = 0^o$ with stiff blades rotor

Changing only the blade set from stiff (Fig. 24) to flexible (Fig. 25) changes some of the $M_{x,p}$ trends discussed above. In the case of flexible blades, the maximum $M_{x,p}$ levels occur at Ω = 600RPM, whereas in the stiff configuration, $M_{x,p}$ reaches its peak at Ω = 750RPM. This change could be attributed to the different amplification of the dominant 2P response by the blade elastic modes. The stiff F1S mode, measured to have a natural frequency of 21 Hz in GVT, contrasts with the flexible blade's frequency of 18.7 Hz. Assuming a stiffening effect due to rotation and minor changes in induction values, the F1S mode amplifies the 2P response more at Ω = 600 RPM (20Hz) for flexible blades and at Ω = 750 RPM (25Hz) for the stiff ones. Lastly, the ϕ region where peak values appear is not affected by the blade set, indicating that the aerodynamic imbalance phenomena are not significantly influenced by the rotational speed variation.

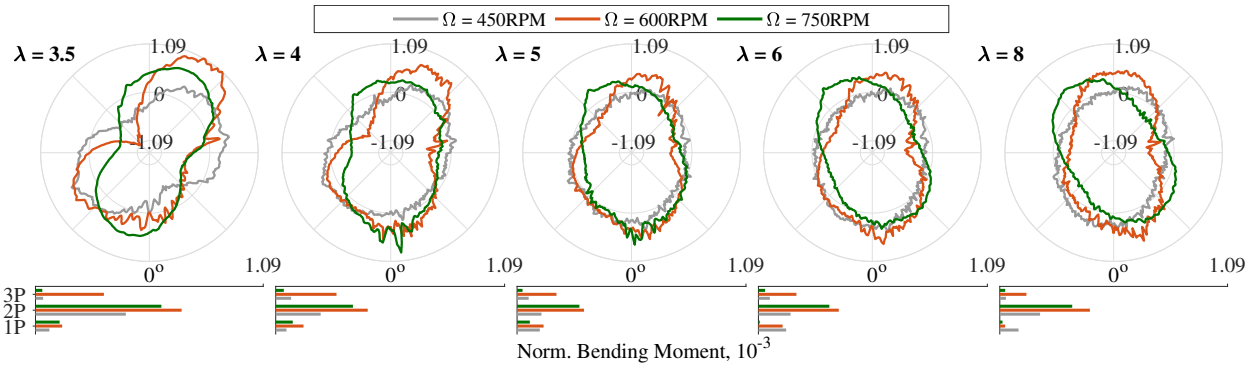

Fig. 25 Dynamic response results, variable rotational speed at $\xi = 60^o$, $\beta = 0^o$ with flexible blades rotor

4. Blade pitch

The last sensitivity parameter to be discussed is β. As β increases from $-2°$ to $0°$, the lift appears to increase, as suggested by the rising C_T in Fig.26. However, there is no discernible change between the $\beta = 0°$ and $+2°$ cases. Conversely, $M_{x,o}$ exhibits a coherent increase of 33% with 2^o increments in β. The highest C_P was observed at the $\beta = -2°$ condition, though it was very close to the $\beta = 0°$ case. Overall, though higher β angles generate more lift, the lift-to-drag ratio is compromised, leading to reduced wind turbine efficiency, as evidenced by the lower levels of C_P. This underscores the anticipated need for optimizing the jig-twist distribution across the rotor's radius to achieve peak performance under design conditions (ξ, Ω, λ).

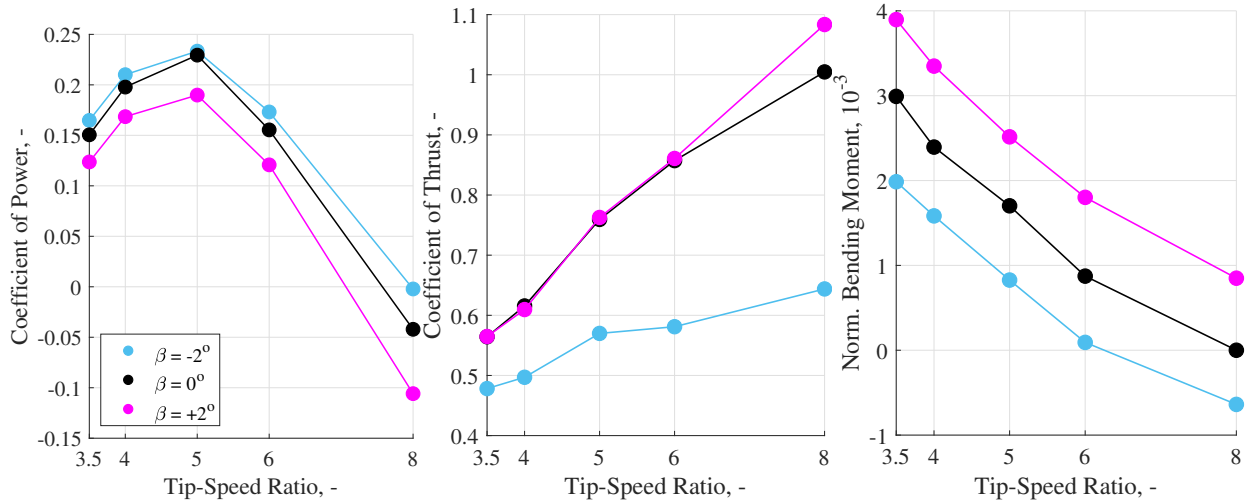

Fig. 26 Static response results, variable blade pitch at $\xi = 60^o$, $\Omega = 600RPM$ with stiff blades rotor

Regarding the dynamic response, β variation had an almost negligible effect, with similar rosette amplitude, orientation, and harmonics as it is observed in Fig.27 across the β range. The only exception is at $\beta = -2°$ and $\lambda = 3.5$ case, where a disproportionate increase of 32% in the 2P component is observed. A possible explanation is that large separation regions at $\beta = 0°$ and $2°$ prevented an increase in loads, while at $\beta = -2°$ the flow remained attached and generated additional lift.

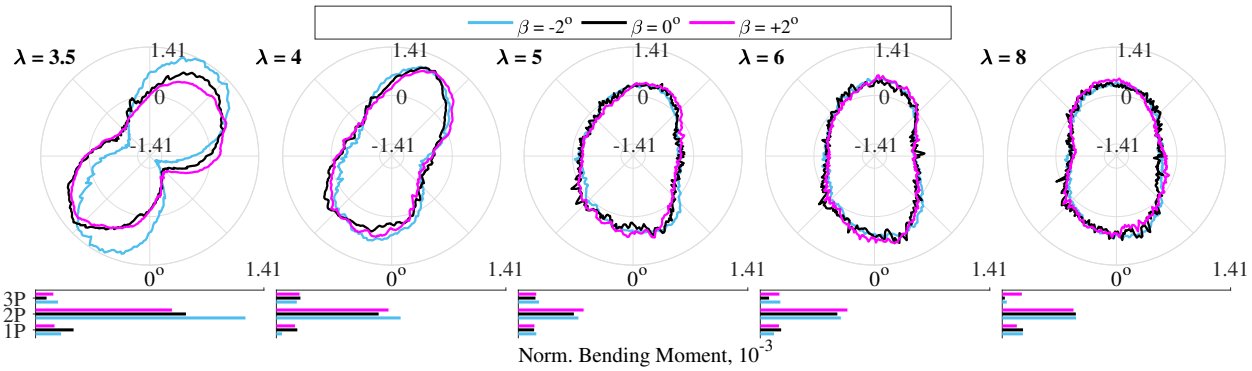

Fig. 27 Dynamic response results, variable blade pitch at $\xi = 60^o$, $\Omega = 600RPM$ with stiff blades rotor

VI. Conclusions

This study conducted an experimental investigation into the aeroelastic behavior and performance of a novel wind turbine concept featuring a yawed teetering rotor. Utilizing a wind turbine model with two distinct sets of elastic blades, following the scaling strategy proposed by Georgopoulos et al. [11], the research aimed to provide valuable insights into the system's static and dynamic aeroelastic response, along with its overall performance. Ground and wind tunnel tests were performed to achieve this objective.

The static tests revealed deviations in static deflection compared to FEM predictions. Notably, flexible blades exhibited a 14% higher flapwise displacement, while stiff blades surpassed predictions by 31%. The mismatch is mainly attributed to rotation at the blade root, imparted by the joining plates. Freeplay at the joints, along with the material's viscoelastic properties, also led to hysteresis between loading and unloading. Symmetric behaviour was observed between blades 1 and 2, with the exception of flexible blades under torsion, as a result of deviations in the application of the film skin.

Dynamic ground vibration tests revealed differences of up to 18.2% between measured and predicted elastic mode natural frequencies, further exposing manufacturing and modelling imperfections. The use of foam to emulate a soft rotational spring at the hinge also introduced exaggerated stiffness, corrupting the measurement of antisymmetric modes. Nevertheless, a significantly improved match between FEM and practice is deemed attainable with a small number of design and modelling adaptations, primarily focused on the joining plates and the film skin.

Wind tunnel tests, conducted with the hinge in fixed and free conditions, supported prior findings regarding lift shape [10]. However, the elastic blades' response was found to be characterized by a 2P component, contrasting with [10] findings that treat the rotor as a rigid body. The delta-3 hinge, placed at $\delta_3 = 63.5^o$, effectively balanced aerodynamic loads between the two blades, arising from the dissymmetry of lift and/or skewed wake effects. Despite the proximity of the 2P frequency to the flexible modes frequencies, no dynamic aeroelastic instability was detected. However, the amplitude of the flexible blades' response was higher at Ω = 600RPM than at Ω = 750RPM, while the opposite was noticed for the stiff set, highlighting the influence of flexible mode amplification factors in the dynamic response of the rotor.

A sensitivity study involving variations in parameters such as ξ, Ω and β, for a range of λ values, highlighted the pronounced influence of λ and Ω on the dynamic aeroelastic response. Specifically, changes in λ altered the azimuthal position and magnitude of maximum loads by 90° and 115%, respectively. Additionally, a notable azimuthal position shift of 60° and a 130% increase in maximum load were observed between Ω = 600 and 750 RPM. Other parameters exhibited a less severe impact on the dynamic response results.

In contrast, the static aerolastic response, mainly monitored by the C_P and C_T coefficients, was not severely affected by Ω. The parameter with the highest impact on the static response was found to be ξ, causing a 56% increase in C_P for $\xi = 60^o$ compared to $\xi = 30^o$ at $\lambda = 5$. The second important parameter was β, where the $\beta = -2^o$ case produced the highest C_P with the lowest static bending moment, indicating operation at a high effective angle of attack for the majority of rotor sections at Ω = 600RPM and $\xi = 60^o$. This highlights the need for optimizing the jig-twist distribution across the rotor's radius in accordance with the intended design conditions.

Key findings of this experimental campaign include the absence of aeroelastic instabilities in this novel configuration under the tested conditions, the effective operation of the delta-3 hinge in balancing aerodynamic loads, the dominance

of the 2P harmonic in the measured blade response and substantial changes in aerodynamics with varying values of λ. Specifically, as λ decreases, the skewed wake effect diminishes, replaced by the dissymmetry of lift, causing a gradual 45^o rotation of the maximum moment azimuthal position in 2P cases and 90^o in 1P cases.

In conclusion, this research provides valuable insights for optimizing the novel teetering and yawed wind turbine rotor design, particularly in addressing construction limitations and refining numerical models to account for elastic blades. While the study highlights the system's robustness and promising performance, it suggests that further research should be conducted, including an exploration of the dynamics of the floating structure and the potential for passive control of the tilt angle.

Acknowledgments

The authors acknowledge support from the Rijksdienst voor Ondernemend Nederland (RVO) through the TSE Hernieuwbare Energie funding scheme for the project "TouchWind-PoP: Proof of principle for cost-effective floating offshore wind turbine concept" (TEHE119017)

References

[1] Bull, D., Fowler, M., and Goupee, A., "A Comparison of Platform Options for Deep-water Floating Offshore Vertical Axis Wind Turbines: An Initial Study," Tech. rep., Sandia National Laboratories, 2014. URL https://api.semanticscholar.org/CorpusID:112209170.

[2] Civati, M., Sartori, L., and Croce, A., "Design of a two-bladed 10 MW rotor with teetering hub," *Journal of Physics: Conference Series*, Vol. 1037, No. 4, 2018. https://doi.org/10.1088/1742-6596/1037/4/042007.

[3] Asim, T., Islam, S. Z., Hemmati, A., and Khalid, M. S. U., "A Review of Recent Advancements in Offshore Wind Turbine Technology," , 1 2022. https://doi.org/10.3390/en15020579.

[4] Borg, M., Shires, A., and Collu, M., "Offshore floating vertical axis wind turbines, dynamics modelling state of the art. part I: Aerodynamics," , 2014. https://doi.org/10.1016/j.rser.2014.07.096.

[5] "TouchWind," , 2023. URL https://touchwind.org/technology/.

[6] Laas, L., "Consortium explores positive wake effects of floating wind turbines," , 2023. URL https://www.tno.nl/en/newsroom/2023/12/wake-effects-floating-windturbines/.

[7] Fagan, E. M., Flanagan, M., Leen, S. B., Flanagan, T., Doyle, A., and Goggins, J., "Physical experimental static testing and structural design optimisation for a composite wind turbine blade," *Composite Structures*, Vol. 164, 2017, pp. 90–103. https://doi.org/10.1016/j.compstruct.2016.12.037.

[8] Bottasso, C. L., Campagnolo, F., and Petrović, V., "Wind tunnel testing of scaled wind turbine models: Beyond aerodynamics," *Journal of Wind Engineering and Industrial Aerodynamics*, Vol. 127, 2014, pp. 11–28. https://doi.org/10.1016/j.jweia.2014.01.009.

[9] Hansen, M. H., Thomsen, K., Fuglsang, P., and Knudsen, T., "Two methods for estimating aeroelastic damping of operational wind turbine modes from experiments," *Wind Energy*, Vol. 9, No. 1-2, 2006, pp. 179–191. https://doi.org/10.1002/we.187.

[10] Krishnan, N., Viré, A., and Klippe, R. V. D., "Study of a passive pitching rotor using blade element momentum theory coupled to a rigid-body model," *Journal of Physics: Conference Series*, Vol. 2265, No. 3, 2022. https://doi.org/10.1088/1742-6596/2265/3/032057.

[11] Georgopoulos, P., Sodja, J., and De Breuker, R., "Design of Flexible Wind Tunnel Model of Yawed Wind Turbine Rotor with Teetering Hub," *AIAA SCITECH Forum*, 2023, p. 2091. https://doi.org/https://doi.org/10.2514/6.2023-2091.

[12] Timmer, W. A., and Van Rooij, R. P., "Summary of the Delft University wind turbine dedicated airfoils," *Journal of Solar Energy Engineering, Transactions of the ASME*, Vol. 125, No. 4, 2003, pp. 488–496. https://doi.org/10.1115/1.1626129.

[13] Hoffmann, K., *An Introduction to Measurements using Strain Gages*, Hottinger Baldwin Messtechnik GmbH, 1989.

[14] Mercker, E., and Wiedemann, J., "On the Correction of Interference Effects in Open Jet Wind Tunnels On the Correction of Interference Effects in Open Jet Wind Tunnels," *Society of Automotive Engineers,JTOR*, Vol. 105, 1996, pp. 795–809. URL https://www.jstor.org/stable/44720797.

[15] Gupta, A., Seiler, P. J., and Danowsky, B. P., "Ground Vibration Tests on a Flexible Flying Wing Aircraft," *AIAA Atmospheric Flight Mechanics Conference*, American Institute of Aeronautics and Astronautics, Reston, Virginia, 2016. https://doi.org/10.2514/6.2016-1753, URL https://arc.aiaa.org/doi/10.2514/6.2016-1753.

[16] Bisplinghoff, R. L., Ashley, H., and Halfman, R. L., *Aeroelasticity*, Dover Publications, Inc, New york, 1996.

[17] Chaney, K., Eggers, A. J., Moriarty, P. J., and Holley, W. E., "Skewed wake induction effects on thrust distribution on small wind turbine rotors," *Journal of Solar Energy Engineering, Transactions of the ASME*, Vol. 123, No. 4, 2001, pp. 290–295. https://doi.org/10.1115/1.1410109.

[18] Chen, J., Shen, X., Zhu, X., and Du, Z., "Influence of wake asymmetry on wind turbine blade aerodynamic and aeroelastic performance in shear/yawed wind," *Journal of Renewable and Sustainable Energy*, Vol. 10, No. 5, 2018. https://doi.org/10.1063/1.5030671.

[19] Bartl, J., Mühle, F., Schottler, J., Sætran, L., Peinke, J., Adaramola, M., and Hölling, M., "Wind tunnel experiments on wind turbine wakes in yaw: Effects of inflow turbulence and shear," *Wind Energy Science*, Vol. 3, No. 1, 2018, pp. 329–343. https://doi.org/10.5194/wes-3-329-2018.